Magnetic resonance elastography: Non-invasive mapping of tissue elasticity

A. Manduca*, T.E. Oliphant, M.A. Dresner, J.L. Mahowald, S.A. Kruse, E. Amromin, J.P. Felmlee, J.F. Greenleaf, R.L. Ehman

Mayo Clinic and Foundation, 200 1ˢᵗ St. SW, Rochester, MN 55901, USA

Abstract

Magnetic resonance elastography (MRE) is a phase-contrast-based MRI imaging technique that can directly visualize and quantitatively measure propagating acoustic strain waves in tissue-like materials subjected to harmonic mechanical excitation. The data acquired allows the calculation of local quantitative values of shear modulus and the generation of images that depict tissue elasticity or stiffness. This is significant because palpation, a physical examination that assesses the stiffness of tissue, can be an effective method of detecting tumors, but is restricted to parts of the body that are accessible to the physician's hand. MRE shows promise as a potential technique for 'palpation by imaging', with possible applications in tumor detection (particularly in breast, liver, kidney and prostate), characterization of disease, and assessment of rehabilitation (particularly in muscle). We describe MRE in the context of other recent techniques for imaging elasticity, discuss the processing algorithms for elasticity reconstruction and the issues and assumptions they involve, and present recent ex vivo and in vivo results. © 2001 Elsevier Science B.V. All rights reserved.

Keywords: Elasticity; Elastography; Strain imaging; Non-invasive palpation; Tumor detection

1. Introduction

There is strong precedent in clinical medicine for the concept that tissue viscoelastic properties, assessed by palpation, are markedly affected by a variety of disease processes. Student physicians learn that the presence of a hard mass in the thyroid, breast or prostate is suspicious for malignancy. Indeed, many tumors of these structures are still first detected by touch. It is not uncommon for surgeons at the time of laparotomy to palpate tumors that were undetected in preoperative imaging by CT, MRI or ultrasound. None of these modalities provide the information about the elastic properties of tissue elicited by palpation. The elastic moduli of various human soft tissues are known to vary over a wide range (more than four orders of magnitude). In contrast, most of the physical properties depicted by conventional medical imaging modalities are distributed over a much smaller numerical range.

Over the last decade, the recognition of the potential diagnostic value of characterizing mechanical properties has led a number of investigators to seek methods for imaging tissue elasticity. In materials science, the classic approach for measuring the elastic modulus of a sample is to apply a known stress and to measure the resulting strain. Refinements of this method involve the use of multiple measurements with varying stress, and/or the application of dynamic rather than static stress. Most of the proposed methods for elasticity imaging follow a similar approach. A stress is applied to tissue and the resulting strain distribution is observed or measured using a conventional imaging technique such as ultrasonography. The mode of stress application can be static, quasi-static, or dynamic. A recent review of such work is given by Gao et al. (1996).

Magnetic resonance elastography (MRE) is a recently developed technique that can directly visualize and quan-

*Corresponding author. Tel.: +1-507-284-8163; fax: +1-507-284-9420.

E-mail address: manduca@mayo.edu (A. Manduca).

titatively measure propagating acoustic strain waves in tissue-like materials subjected to harmonic mechanical excitation (Muthupillai et al., 1995, 1996a). Shear waves at frequencies in the 10–1000 Hz range are used as a probe because they are much less attenuated than at higher frequencies, their wavelength in tissue-like materials is in the useful range of millimeters to tens of millimeters, and because shear modulus varies widely in bodily tissues. A phase-contrast MRI technique is used to spatially map and measure the shear wave displacement patterns. From this data, local quantitative values of shear modulus can be calculated and images (elastograms) that depict tissue elasticity or stiffness can be generated. In this paper we briefly summarize other techniques for imaging elasticity and describe the principles of MRE. We then consider the equations of harmonic motion in soft tissue and describe various approaches for reconstructing elastograms from MRE data and the assumptions inherent in each. These algorithms are then tested on synthetic and physical phantom data sets of known stiffness and issues such as noise sensitivity and resolution are discussed. Finally, a summary of recent ex vivo and in vivo results is presented.

2. Elastic properties of soft tissue

It is ironic that while the elastic properties of structural materials have been extensively characterized by engineers and physicists for more than a century, these properties are virtually unknown for biological soft tissues. The scarcity of such data in the literature most likely stems from the technical difficulty of measuring the elastic properties of semisolid biologic tissues using conventional laboratory methods such as mechanical load-cell testing devices, which rely on well-defined boundary conditions (Fung, 1993). While limited, this data does indicate that quantitative measurements of mechanical properties may be useful in distinguishing between benign and malignant tissues. For example, data from breast tissue specimens have consistently shown that the measured shear moduli of various types of carcinomas are much higher than the shear moduli of normal adipose-glandular tissue (Sarvazyan et al., 1994; Burke et al., 1990; Krouskop et al., 1998). It is generally agreed that no other physical parameter of tissue is changed by pathological or physiological processes to as great an extent as its elasticity.

In isotropic tissues, the proportionality constant that describes the amount of longitudinal deformation (expressed in terms of strain) that occurs in a given material in response to an applied longitudinal force (expressed in terms of stress) is known as *Young's modulus* (E) of elasticity. The *shear modulus* (μ) relates transverse strain to transverse stress. Similarly, the *bulk modulus* (K) of elasticity describes the change in volume of a material to external stress. Another physical property of isotropic Hookean solids is *Poisson's ratio* (v), which is the ratio of

transverse contraction per unit breadth divided by longitudinal extension per unit length. These parameters are interrelated, so that knowledge of any two allows calculation of the other two.

Most soft tissues have mechanical properties that are intermediate between those of fluids and solids. The value of Poisson's ratio for soft tissues is in the range of $v = 0.490$–0.499, which is very close to the value for liquids ($v = 0.500$). In this case the Young's modulus and shear modulus differ only by a scaling factor ($E = 3\mu$). Another characteristic that soft tissues share with liquids is that they are nearly incompressible. In contrast to the many orders of magnitude over which the Young's and shear moduli are distributed, the bulk moduli of most soft tissues differ by less than 15% from that of water (Goss et al., 1978). The density of soft tissue also differs little from that of water (Burlew et al., 1980).

These concepts represent a simplification of the mechanical behavior of soft tissues, which in general can be anisotropic, non-Hookean and viscoelastic.

3. Elasticity imaging techniques

Much of the pioneering work in elasticity imaging has been accomplished using ultrasound and either a quasi-static stress model (Ophir et al., 1991; O'Donnell et al., 1994; Cespedes et al., 1993; Garra et al., 1997) or a dynamic stress model (Gao et al., 1995; Huang and Roach, 1991; Lee et al., 1991; Lerner et al., 1990; Parker et al., 1990; Parker and Lerner, 1992; Rubens et al., 1995).

The quasi-static stress method employs an ultrasound transducer to apply a small axial compression to tissue. Sonograms obtained without and with compression are correlated to determine the displacement at each location, thereby revealing the longitudinal strain distribution. The local strain is a relative measure of elasticity since it depends on the magnitude of compression and on the elastic modulus of the material. Images depicting this local strain estimate have been shown to provide an informative qualitative depiction of the elasticity of materials in tissue-simulating phantoms and surgical tissue specimens (O'Donnell et al., 1994). In vivo studies of the method have demonstrated the feasibility of delineating breast cancer (Cespedes et al., 1993) by elastography. Such images can also be processed to compute a quantitative map of regional elastic modulus (E). The calculation requires an estimate of local stress distribution, which in turn depends on the spatial composition of the object and knowledge of the applied stress distribution (Ponnekanti et al., 1992, 1994, 1995).

The sonoelasticity method developed by Parker and coworkers (Parker et al., 1990; Parker and Lerner, 1992) employs a vibrational mechanical stress, typically in the range of 20–400 Hz. Tissue is imaged with Doppler ultrasonography to observe the regional amplitude of the

resulting standing wave pattern. Structures with high elastic moduli tend to have lower vibrational amplitudes than surrounding softer tissues. An in vitro study of excised prostates has demonstrated that this qualitative technique delineates adenocarcinoma with higher sensitivity than conventional sonographic imaging (Rubens et al., 1995). A related method has employed Doppler ultrasound in an attempt to map the pattern of propagating mechanical waves in phantoms, animal tissue, and in the human liver (Yamakoshi et al., 1990; Krouskop et al., 1987).

Other investigators have recently proposed several approaches for delineating tissue elasticity using MRI. One approach is to employ saturation tagging methods, which have been used in applications as diverse as evaluating the local motion of cardiac muscle (Axel and Dougherty, 1989; Zerhouni et al., 1988) and observing connective motion in vibrated granular material (Ehrichs et al., 1995). A proposed method is to apply a grid of saturation tags to tissue before it is deformed by an applied static stress (Fowlkes et al., 1995). The pattern of deformation of the grid of saturation tags could then be analyzed to provide a map of local strain. A mathematical model of stress distribution within the object could also be used, in principle, to convert this map of local strain into a quantitative depiction of regional elastic modulus.

Another well-known MRI method for measuring local motion is motion-encoded phase-contrast imaging. This has been used clinically in applications such as assessing regional myocardial motion, CSF pulsation, and intravascular blood flow (O'Donnell, 1985; Bernstein and Ikezaki, 1991; Pelc et al., 1989). Plewes and colleagues proposed a method for elastography involving use of a phase-contrast imaging sequence to estimate the spatial strain distribution resulting from a small quasi-static longitudinal stress, applied once each time the pulse sequence is repeated (Plewes et al., 1994, 1995). Phantom studies showed that the strain maps allow distinction of an object with high stiffness from surrounding softer material. Again, a quantitative determination of the regional elastic modulus can be calculated given an estimation of the regional distribution of stress.

4. Magnetic resonance elastography (MRE)

MRE uses propagating mechanical waves rather than static stress as a probe. This provides major advantages in calculating elasticity because it does not require estimation of the regional static stress distribution. Shear waves at frequencies in the 50–1000 Hz range are suitable as a probe because they are much less attenuated than at higher frequencies, their wavelength in tissue-like materials is in the useful range of millimeters to tens of millimeters, and because shear modulus varies so widely in bodily tissues. High frequency longitudinal acoustic waves (ultrasound) are not directly suitable for use as a probe, because their propagation is governed by the bulk modulus, which varies little in soft tissue. Longitudinal acoustic waves at lower frequencies are also not suitable because they have a long wavelength (on the order of meters below 1 kHz) (Goss et al., 1978).

In MRE, a phase-contrast MRI technique is used to spatially map and measure displacement patterns corresponding to harmonic shear waves with amplitudes of microns or less. A conventional MRI system is used with an additional motion-sensitizing gradient imposed along a specific direction, switched in polarity at some adjustable frequency (Fig. 1). Trigger pulses synchronize an oscil-
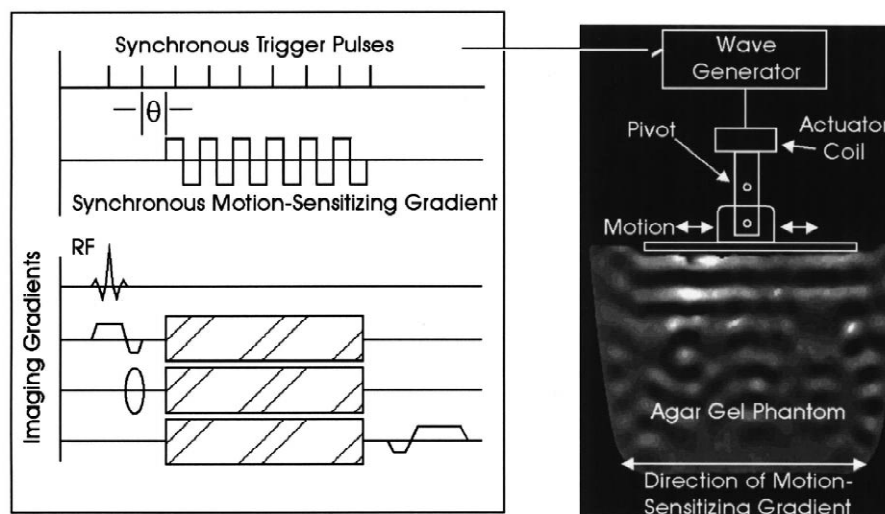

Fig. 1. Schematic diagram of magnetic resonance elastography system. Conventional MR imaging gradients and RF pulses that encode spatial positions are shown at the bottom left. The electromechanical driver applies transverse acoustic waves to the object to be imaged via a surface plate (right). The cyclic motion-sensitizing gradients and the acoustic drive are synchronized using trigger pulses provided by the imager. The phase offset (θ) between the two can be varied. As shown by the shaded regions, the motion-sensitizing gradients can be superimposed along any desired axis to detect cyclic motion.

lator/amplifier unit that drives an electromechanical actuator coupled to the surface of the object to be imaged, inducing shear waves in the object at the same frequency as the motion-sensitizing gradient. Any cyclic motion of the spins in the presence of these motion-sensitizing gradients causes a measurable phase shift in the received MR signal. From the measured phase shift, it is possible to calculate the displacement at each voxel, and directly image the acoustic waves within the object.

The phase shift caused by a propagating mechanical wave with a wave vector k within a medium at a given frequency $(1/T)$ in the presence of a cyclic motion-encoding gradient is given by (Muthupillai et al., 1995, 1996a)

$$\phi(\vec{r}, \theta) = \frac{\gamma N T (\vec{G}_0 \cdot \vec{\xi}_0)}{2} \cos(\vec{k} \cdot \vec{r} + \theta). \qquad (1)$$

This accumulated phase shift is proportional to the dot product of the displacement amplitude vector $\vec{\xi}_0$ and the motion-sensitizing magnetic gradient vector $\vec{G}_0$, and the relative phase θ of the mechanical and magnetic oscillations. Particles whose component of motion along the gradient vector are exactly in phase or out of phase with the magnetic oscillation have maximum phase shifts of opposing polarities. Particles whose component of motion along the gradient vector is 90° out of phase with it have no net phase shift. Since the response is also proportional to the number of gradient cycles (N) and the period of the gradient waveform (T), extreme sensitivity to small amplitude synchronous motion can be achieved by accumulating phase shifts over multiple cycles of mechanical excitation and the motion-sensitizing gradient waveform. The quantity γ is the gyromagnetic ratio and $\vec{r}$ is the spin position vector.

Generally, two acquisitions are made for each repetition, in an interleaved fashion reversing the polarity of the motion-sensitizing gradients. This reduces systematic phase errors and doubles the sensitivity to small displacements. In many of our experiments, the direction of the motion-sensitizing gradients is collinear with the direction of motion and perpendicular to the direction of initial wave propagation. Typical data acquisition parameters for 2D sequences are: TR: 10–300 ms, TE: 10–60 ms, acquisition matrix 128–256, acquisition time 20–120 s, flip angle 10–60°. The number of gradient pulses (N) varies from two to 30 cycles and the frequency of mechanical excitation ranges from 50 to 1000 Hz. Acquiring and processing 2D slices captures only two of the three components of the wave propagation vector, and may yield misleading results unless the shear wave is propagating in plane, but in some cases time considerations or other factors mandate their use. 3D MRE pulse sequences have also been developed (Muthupillai et al., 1997) and are increasingly being utilized.

The resulting images reflect the displacement of spins due to acoustic strain wave propagation in the medium and are termed 'wave images'. Such an image of propagating acoustic waves in a tissue-simulating agarose gel phantom is shown in Fig. 2(a). The local wavelength of the propagating waves depends on the elasticity of the material at each location in the object, allowing the construction of elastograms (Fig. 2(b)). Experiments to assess the sensitivity of the shear wave imaging method at low amplitudes of mechanical excitation demonstrated that shear waves with displacements of less than 100 *nanometers* can be readily observed (Muthupillai et al., 1995).

Most of our experiments have been conducted with a moving-coil driver with the imager providing the static magnetic field. Trigger pulses are provided by the sequencing computer of the MR imager, and are fed to a function generator which generates a waveform that is amplified and applied to the coil of the actuator. Transverse stresses applied to a flat contact plate provide planar shear waves. Contact friction between a plastic plate and human skin is sufficient to transfer shear motion across the interface. Piezoelectric drivers can also be used for generating shear waves. These have high force output and can be freely oriented within the magnetic field, but have a limited maximum displacement and do not offer significant advantages over the moving-coil design. Focused ultrasound can also be used to generate shear waves that can be imaged with MRE (Wu et al., 2000). The ultrasound beam is temporally modulated to create cyclic variation in acoustic radiation pressure at the focus of the ultrasound source, which can be localized deep within an object. Good agreement has been found between the shear modulus measured from MRE images using focused ultrasound for shear excitation and using conventional drivers.

By adjusting the phase offset between the mechanical excitation and the oscillating magnetic gradient (θ in Fig. 1), acoustic wave images can be obtained at various phase offsets regularly spaced around a cycle. This allows extraction of the harmonic component at the frequency of interest, giving the amplitude and the phase (relative to an arbitrary zero point) of the harmonic displacement at each point in space (Manduca et al., 1997a). This complex displacement field is the input to all the processing techniques described below. This extraction also provides some degree of noise reduction and allows visualization of wave propagation as a cine loop. Four to eight phase offsets are typically captured in most experiments.

A single MRE acquisition captures only one component of the displacement data; i.e., it is sensitized to motion in a single direction. However, the experiment can be repeated and the sensitization direction varied, to capture all three orthogonal components of displacement. Thus, the data set acquired by MRE can be very rich: full 3D cyclic displacement information can be acquired at MR pixel resolution throughout a 3D volume. In principle, this makes it feasible to estimate all components of the strain dyadic, thereby making it possible to probe the anisotropic mechanical properties of tissues (Muthupillai et al., 1995,
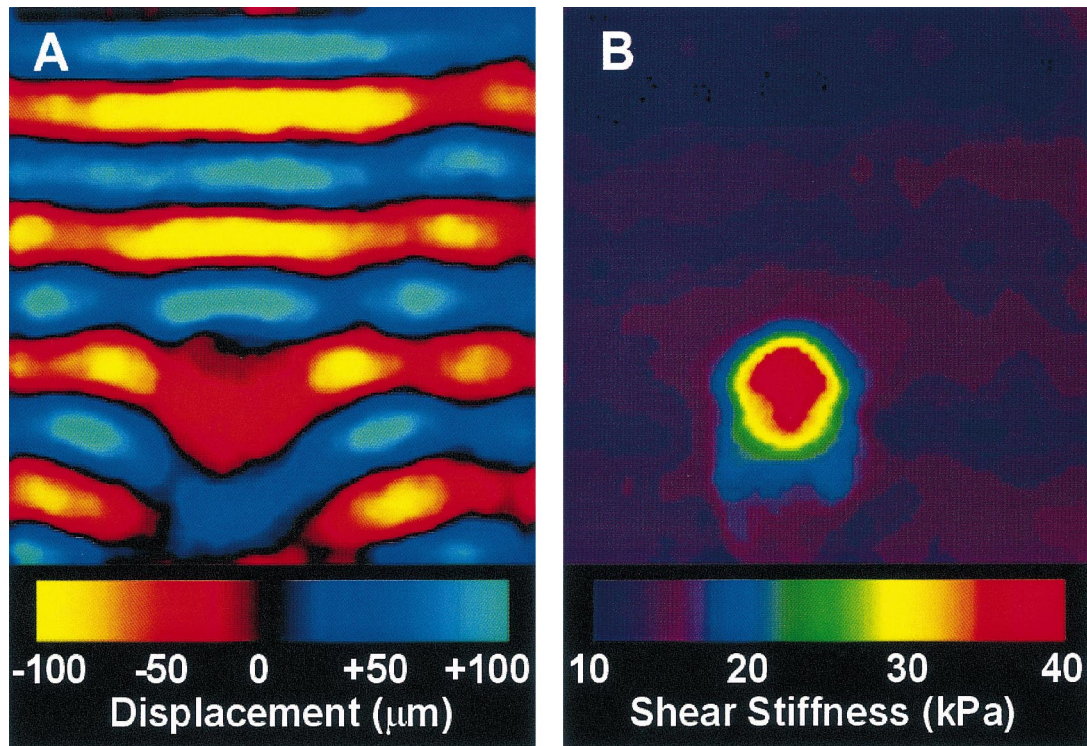
Fig. 2. Object with diameter comparable to wavelength. (a) Shear waves propagating in a phantom with an embedded 1.5 cm diameter cylinder of stiffer gel. Shear waves at 300 Hz were applied at the top margin of the gel block, with transverse motion oriented orthogonal to the plane of the image. (b) The elastogram based on LFE processing clearly depicts the object, even though it is relatively small in comparison to the wavelength.

1996a; Kruse et al., 2000). MRE also benefits from a freely oriented field of view unencumbered by the 'acoustic window' required for ultrasound-based techniques.

Given the sensitivity of the MRE method to cyclic motions with amplitudes as small as 100 nm (less than the wavelength of light), one might wonder whether the technique will be inordinately sensitive to physiologic motion. We have found that it is highly sensitive only to motion that is precisely synchronized with the sensitization gradients, and is little more sensitive to physiologic motion than a conventional gradient echo sequence (Muthupillai et al., 1996b). Sensitivity to non-synchronous motion can be further reduced by explicitly nulling the individual moments of the gradient waveform. It is also possible to amplitude modulate (apodize) the envelope of the motion-encoding waveform to further increase its spectral selectivity (Muthupillai and Ehman, 1997). Our results to date have not revealed any undue limitations due to physiologic motion.

In summary, MRE offers: direct visualization and quantitative measurement of tissue displacements, high sensitivity to very small motions, a field of view unencumbered by acoustic window requirements, and the ability to obtain full 3D displacement information throughout a 3D volume. As shown below, under some assumptions this allows direct local inversion of the data to recover elasticity, with no need for boundary conditions or the estimation of a stress field.

5. Data processing

A variety of approaches can be used to invert the displacement data to recover mechanical properties. These are characterized below by the assumptions or simplifications made in their derivations. It is possible to deduce quantitatively accurate values of properties such as shear modulus in favorable situations. In general, however, despite the richness of the data set and the variety of processing techniques, it remains a challenge to extract accurate results at high resolution in complex, heterogeneous objects from the intrinsically noisy data.

5.1. Equations of motion

The mechanical quantities we wish to characterize are those that relate the strain to stress, and since the displacements in MRE are very small (on the order of microns), a linear relationship can be assumed between these. In the general case, stress and strain are related by a rank 4 tensor with up to 36 independent quantities (Auld, 1990). If one assumes that the material is isotropic, this reduces to two independent quantities, the Lame constants λ and μ, related to longitudinal and shear deformation respectively. The isotropic relation between stress and strain is given by

$$\sigma_{ij} = 2\mu e_{ij} + \lambda \delta_{ij} e_{nn}, \tag{2}$$

where e_{ij} is one component of the stress tensor, δ_{ij} is the Kronecker delta, and summing over repeated indices is assumed. The strain tensor e_{ij} is defined in terms of the displacement tensor u_{ij} as

$$e_{ij} = (u_{i,j} + u_{j,i})/2, \tag{3}$$

where indices after a comma indicate differentiation. Substituting these into the equation of motion, we obtain the general equation for harmonic motion in an isotropic, linearly elastic medium (Kallel and Bertrand, 1996),

$$[\lambda u_{j,j}]_{,i} + [\mu(u_{i,j} + u_{j,i})]_{,j} = -\rho\omega^2 u_i, \tag{4}$$

with ρ the density of the material and ω the angular frequency of the mechanical oscillation. The Lame constants can be considered to be complex quantities, with the imaginary parts of the constants representing attenuation for a viscoelastic medium. Solving this equation requires knowledge of the full 3D displacement, since the equations for the individual components are coupled. MRE phase difference measurements in all three spatial orientations are thus required.

Additional assumptions can be made to further simplify the equation. If one assumes local homogeneity, λ and μ become single unknowns instead of functions of position, and (4) becomes an algebraic matrix equation that can be solved locally by direct inversion as described below (terms in boldface are column vectors):

$$\mu\nabla^2\boldsymbol{u} + (\lambda + \mu)\nabla(\nabla\cdot\boldsymbol{u}) = -\rho\omega^2\boldsymbol{u}. \tag{5}$$

In soft tissues, $\lambda \gg \mu$ (typically 10^4 or more). This makes it difficult to estimate both parameters simultaneously, but it also effectively decouples the two. It is possible to partially filter out the effects of the longitudinal wave since its contributions are at very low (near zero) spatial frequency. Filtering approaches can also be designed based on the fact that the displacement field corresponding to the longitudinal wave is curl-free, while that corresponding to the shear wave is divergence-free. In general, the longitudinal wavelength is so long in tissues (tens of meters) that accurate estimation of λ is very challenging.

To remove λ from consideration, the assumption can be made that displacements due to the longitudinal wave vary slowly and thus are negligible (this corresponds to assuming that $\lambda(\nabla\cdot\boldsymbol{u}) = 0$). The large differences between longitudinal and shear waves in tissue make this a reasonable assumption. The equation then simplifies to a single vector equation in μ, but all three components of motion are still required:

$$[\nabla(\nabla\cdot\boldsymbol{u})\nabla^2\boldsymbol{u}]\mu = -\rho\omega^2[\boldsymbol{u}]. \tag{6}$$

Alternatively, one can assume incompressibility ($\nabla\cdot\boldsymbol{u} = 0$), and the equation then simplifies to the Helmholtz equation,

$$\mu\nabla^2\boldsymbol{u} = -\rho\omega^2\boldsymbol{u}. \tag{7}$$

Importantly, the terms involving components in the different orthogonal directions are now decoupled, and each component satisfies the equation separately. Thus, measurements in only one sensitization direction (and an estimate of the Laplacian of that component) suffice to determine μ.

5.2. Shear modulus and mechanical frequency

In the treatment above, the Lame constants are complex quantities, with the imaginary parts representing attenuation for a viscoelastic medium. Since the damping term involves the time derivative of the strain, for harmonic motion this can be denoted as $\mu = \mu_r + i\mu_i = c + i\omega\eta$ (Auld, 1990). Let us consider the simplest case: that of an isotropic, homogeneous, incompressible medium (Eq. (7)). With no attenuation, a simple shear wave propagates with a specific wavelength or spatial frequency f_{sp}. The shear modulus is $\mu = \rho f^2_{mech}/f^2_{sp} = \rho v_s^2$, where f_{mech} is the mechanical driving frequency and v_s is the wave speed (or phase velocity). We will henceforth assume that $\rho \sim 1.0$ for all soft tissues (Burlew et al., 1980). If there is attenuation, the wave speed and attenuation are functions of frequency, and are given by

$$v_s^2 = \frac{2(c^2 + \omega^2\eta^2)}{c + (c^2 + \omega^2\eta^2)^{1/2}} \tag{8}$$

and

$$\alpha^2 = \frac{\omega^2}{2}\frac{(c^2 + \omega^2\eta^2)^{1/2} - c}{c^2 + \omega^2\eta^2}, \tag{9}$$

where α denotes attenuation by the factor $e^{-\alpha k}$ in the direction of propagation k. The attenuation can also be expressed as the attenuation per wavelength, which is the acoustic quality factor $Q = c/\omega\eta$ (Auld, 1990).

The true 'shear modulus' is the real part μ_r or c, which describes the behavior of a static object in equilibrium. However, some processing techniques (LFE, phase gradient) calculate only the local wavelength and do not treat attenuation. These techniques essentially estimate the wave speed, and we can speak of an 'effective' shear modulus or 'shear stiffness' that is defined as the square of the wave speed by analogy to the lossless case. The results below are usually presented in terms of this shear stiffness at a given frequency.

Other techniques (AIDE) calculate both μ_r and μ_i (or c and η) directly, which can be converted to wave speed and attenuation using Eqs. (8) and (9) above. This determination of μ_i or α tends to be very sensitive to noise. A more stable way to determine the c and η parameters is to calculate the shear stiffness at several different frequencies and fit the result to expressions derived from (8) and (9).

The spatial wavelength and shear stiffness decrease and increase respectively as the mechanical frequency increases, and attenuation increases. From the point of view

of stiffness determination, this has two competing effects: (1) higher resolution, since the wavelength is smaller, but (2) higher attenuation, implying lower signal. The best frequency for a particular application depends on this tradeoff.

5.3. Local frequency estimation (LFE)

Our initial processing approach was based on estimating the local spatial frequency of the shear wave propagation pattern, using an algorithm that combines local estimates of instantaneous frequency over several scales (Knutsson et al., 1994). These estimates are derived from filters that are a product of radial and directional components and can be considered to be oriented lognormal quadrature wavelets. The shear stiffness is then $\mu = f_{mech}^2 / f_{sp}^2$, with the assumption that $\rho \sim 1.0$ for all soft tissues. It can be shown that this approach is solving the Helmholtz equation obtained under the assumptions of local homogeneity, incompressibility, and no attenuation. The LFE allows estimation of μ from a single image; i.e., using displacement values for a single sensitization direction and a single phase offset. It is equally applicable to the complex harmonic displacement extracted from multiple phase offsets.

The LFE algorithm has proven to be a robust, useful technique because of the sophisticated multi-scale data averaging in the estimation. It yields accurate and isotropic local frequency estimates and is relatively insensitive to noise (Manduca et al., 1996), and is easily extended to 3D (Manduca et al., 1997b). One disadvantage is the limited resolution; at sharp boundaries the LFE estimate is blurred, and the correct estimate is reached only half a wavelength into a given region. If one considers a stiff object of size equal to (say) an eighth of a spatial wavelength embedded in a less stiff background material, the LFE estimate of μ for the object will never reach the correct value. However, the object is *detectable*; that is, the existence of a stiff object is evident even if quantitative determination of its stiffness is inaccurate.

5.4. Phase gradient

After extracting the harmonic component at the driving frequency, one has both an amplitude and a phase (relative to an arbitrary zero point) that characterize the harmonic oscillation at each pixel in the image. If the motion is a simple shear wave, the gradient of this phase is precisely the quantity we seek: the change in phase per pixel, easily convertible to a local frequency and thus to shear stiffness as above. In principle, this analysis can have very high resolution, but it is very sensitive to noise, and some averaging of the gradient is usually necessary. This technique yields inaccurate results when two or more waves are superimposed (e.g. reflected waves) or when the motion is complex, since the phase values do not then

represent a single propagating wave (Catheline et al., 1999). However, it is useful in situations where simple plane wave propagation is a good approximation. It should be noted that the LFE and AIDE techniques do not suffer from this drawback; they correctly handle reflections and other complex interactions since they are based on the underlying equations of motion.

5.5. Algebraic inversion of the differential equation (AIDE)

Algebraic inversion of the differential equation (AIDE) is our term for the direct inversion of the motion equations (5)–(7) assuming local homogeneity (Oliphant et al., 1999, 2000). These equations can be solved separately at each pixel using only data from a local neighborhood to estimate local derivatives. *Full AIDE inversion* of (5) estimates both Lame coefficients for an isotropic material and requires all the components of motion. If we rewrite (5) as

$$A \begin{bmatrix} \lambda + \mu \\ \mu \end{bmatrix} = -\rho\omega^2 \begin{bmatrix} u_1 \\ u_2 \\ u_3 \end{bmatrix},$$

$$\text{where } A = \begin{bmatrix} A_{11} & A_{12} \\ A_{21} & A_{22} \\ A_{31} & A_{32} \end{bmatrix} = \begin{bmatrix} u_{i,i1} & u_{1,ii} \\ u_{i,i2} & u_{2,ii} \\ u_{i,i3} & u_{3,ii} \end{bmatrix}, \quad (10)$$

then the solution is given by

$$\begin{bmatrix} \lambda + \mu \\ \mu \end{bmatrix} = -\rho\omega^2 (A^*A)^{-1} A^* \begin{bmatrix} u_1 \\ u_2 \\ u_3 \end{bmatrix}, \quad (11)$$

where A^* is the conjugate transpose of the matrix A. Assuming that the longitudinal pressure varies slowly (so its derivative is negligible; Eq. (6)), the inversion is given by (11) without the λ term. This still requires all polarizations of motion. Assuming an incompressible material (7) gives *incompressible AIDE*, or *Helmholtz inversion*, which allows estimation of shear modulus from a single polarization of motion,

$$\mu = -\rho\omega^2 \frac{u_i}{\nabla^2 u_i}. \quad (12)$$

Again, ρ is assumed to be 1.0 for all soft tissues. A separate assumption path (Oliphant et al., 2000) can be used for 2D imaging by assuming that all derivatives in the out-of-plane direction are negligible. The shear mode then decouples and can be solved by 2D Helmholtz inversion from the out-of-plane shear motion component only.

In practice, all the AIDE techniques require data smoothing and the calculation of accurate second derivatives from the noisy data. In our current implementation, both of these are done by convolution with Savitzky–Golay filters (Press et al., 1992). An alternative approach

also used fits the data to specific quadratic forms with analytic derivatives.

It should be emphasized that the AIDE techniques do not depend on planar shear wave propagation, but simply on the presence of motion (that satisfies the assumed physical model) in the region of interest. In particular, complex interference patterns from reflection, diffraction, etc. do not pose difficulties, except that these patterns may contain areas of low amplitude and hence low SNR. This is also true for the LFE algorithm, which despite its origin as an image processing method is actually inverting the Helmholtz equation (with the additional assumption of no attenuation) and correctly handles superimposed waves.

5.6. Variational method

Romano et al. (1998) have suggested using the weak (variational) form of (4) above and appropriately chosen test functions to estimate the Lame coefficients. This 'variational' method avoids derivative calculations by taking analytic derivatives of smooth test functions and integrating these over local windows in product with the data. In practice, this is similar to our methods of derivative calculations (by filtering with the derivative of a smooth function). Their assumption of constant μ/ρ also is essentially equivalent to our local homogeneity assumption. Thus this approach, while providing valuable insights, is essentially equivalent to AIDE, and we have confirmed this with results obtained implementing this method.

5.7. Solving the inhomogeneous differential equation

The assumption of local homogeneity is used to simplify the equation in the techniques above. This necessarily implies inaccurate results at or near the boundaries between regions and a limit to resolution on the order of the local window size. A different possibility is to not make this assumption, and solve Eq. (4) allowing the mechanical properties to vary in the physical model. This has two confounding effects: (1) the equation remains a differential equation and not an algebraic one, and (2) the assumption of incompressibility does not decouple the equations of motion for shear modulus, so all components of motion are once again necessary. This approach is computationally more challenging but in principle more accurately models the physics of motion for arbitrary materials.

5.7.1. Finite element analysis

Van Houten et al. (1999) recently described a finite element based subzone technique for solving this equation. In their approach, a solution is iteratively refined on small overlapping subzones of the overall domain, by updating the solution based on differences between forward calculations of displacement from the current solution and measured values. After an update is performed on one subzone, the subzone with the greatest residual error is determined and updated next. The approach is elegant and impressive results have been demonstrated on synthetic 2D data with noise. Attenuation has not yet been treated, and calculation times in 3D may become an issue. The results shown to date on actual acquired data are poor, apparently because these are acquired in a transient mode and the model is assuming equilibrium. Nonetheless, this remains an attractive framework in which to solve the problem, and we are exploring similar schemes.

5.7.2. Direct solution

The approach above iteratively solves the forward problem until suitable agreement is found between the measured and computed displacement. A second idea is to develop computationally efficient ways to obtain direct solutions of Eq. (4). We are studying a variety of approaches to this. For all of these methods the parameters of the differential equation (displacement and its derivatives) are known only through noisy measurement, so regularization of some kind is necessary. This regularization takes the form of added constraints to the inversion problem based on assumptions of the expected result, such as its regularity or piecewise uniformity.

5.8. Signal-to-noise considerations

It is important to understand whether there is sufficient signal in a given region to yield an accurate stiffness estimate, and what the uncertainty is in that estimate. In MRE, 'signal' means not only MR signal but, more importantly, that the region is undergoing sufficient motion that the induced phase shifts can be detected and well quantified.

A simple model of how noise in the MR acquisition translates to noise in the phase difference or 'wave' images can be derived. The noise level in the standard MR magnitude image reconstructed from the MRE acquisition can be determined from the background (after correction for rectification). In areas of significant magnitude, this noise can be considered to be Gaussian in both the real and imaginary components. Thus, it forms a Gaussian cloud about the true magnitude and phase, and the uncertainty in phase for a given noise level and magnitude can be calculated. In the wave images, this uncertainty in phase is the noise, and the signal is the accumulated phase shift due to motion. Local SNR in the wave images can thus be determined. Higher SNR is obtained by (1) a larger underlying MR magnitude signal, and (2) a larger displacement amplitude, leading to a larger accumulated phase shift.

The effect of a given SNR in the wave images on shear modulus estimations depends on the actual shear modulus and on the processing algorithm used. All inversion techniques need to estimate derivatives of the displacement. In a stiffer material, the shear wave has a longer wavelength, making the derivatives smaller and the effects
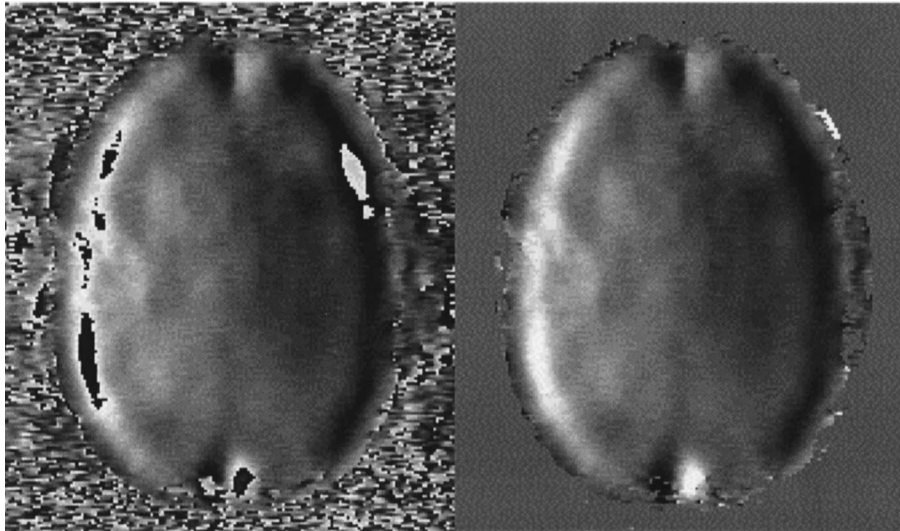
Fig. 3. A phase wrapped wave image of propagating shear waves in the brain and the image after phase unwrapping and masking. Shear waves were generated in the brain at 100 Hz by applying lateral motion to a thermoplastic bite bar held in the teeth of the volunteer. The elastogram calculated from this data is shown in Fig. 15.

of noise more serious. Synthetic wave images with regions of different wavelengths (and thus, effectively, shear moduli) and differing levels of Gaussian noise can be used (as illustrated on test data sets below) to estimate the uncertainty in the shear modulus determinations *due to noise alone*.

5.9. Phase unwrapping

Since shear waves attenuate quickly in certain tissues, large amplitudes near the surface may be required to achieve sufficient amplitude in a deep region of interest. Too much amplitude can cause phase wrap; i.e., large enough displacements can cause accumulated phase shifts outside the range $\pm\pi$, which are ambiguous. This sets an upper limit to the amplitude at which the tissue should be driven. However, standard phase unwrapping algorithms (Ghiglia and Pritt, 1998) can be applied to MRE data with good success, since the wrapped regions are usually fairly well localized (Fig. 3). The upper limit on amplitude can then be increased as long as the phases can be reliably unwrapped. While the optimal unwrapping algorithm and its limits are still under investigation, we have successfully unwrapped images with two nested phase wraps. This translates to a $5\times$ increase in maximum useful amplitude and thus SNR. Alternatively, the increased amplitude can be traded off for higher resolution by operating at a higher mechanical frequency.

6. Results on test data

To illustrate the different noise sensitivity, resolution and accuracy of the various processing techniques, we present results on synthetic and physical phantoms of known parameters.

6.1. Two-region image

The first phantom is a 2D data set that simulates a perfect plane shear wave propagating through two homogeneous regions separated by a sharp boundary. The two regions have no attenuation and their simulated shear moduli are 25.0 and 6.25 kPa. Eight phase offsets were simulated of three data sets: without noise, with Gaussian noise added to simulate a wave image SNR of 5:1, and a noise-smoothed (median filtered) version of the latter. In most of our experiments, the wave images achieve SNR levels of better than 5:1, so this represents a realistic but fairly noisy situation. These data sets are not simulations of physical wave propagation or the MRE acquisition process, but simply sinusoidal wave patterns with noise added.

Fig. 4 shows the results of the LFE, phase gradient and AIDE reconstructions for the three data sets. With no noise, all the techniques yield accurate results, and the LFE has a blurrier boundary than the phase gradient and AIDE algorithms. Both of the latter were calculated using 11×11 local windows. Fig. 5 shows profiles through the reconstructions. The LFE is smoother than the others, but again has lower resolution. The AIDE reconstruction, conversely, is sharper but more sensitive to noise. The phase gradient result has perhaps the best combination of sharp boundary and low noise sensitivity. To some extent, the latter two techniques can trade off resolution against noise sensitivity by altering the size of the local window. All three techniques assume local homogeneity, which breaks down when the boundary between the regions is within the
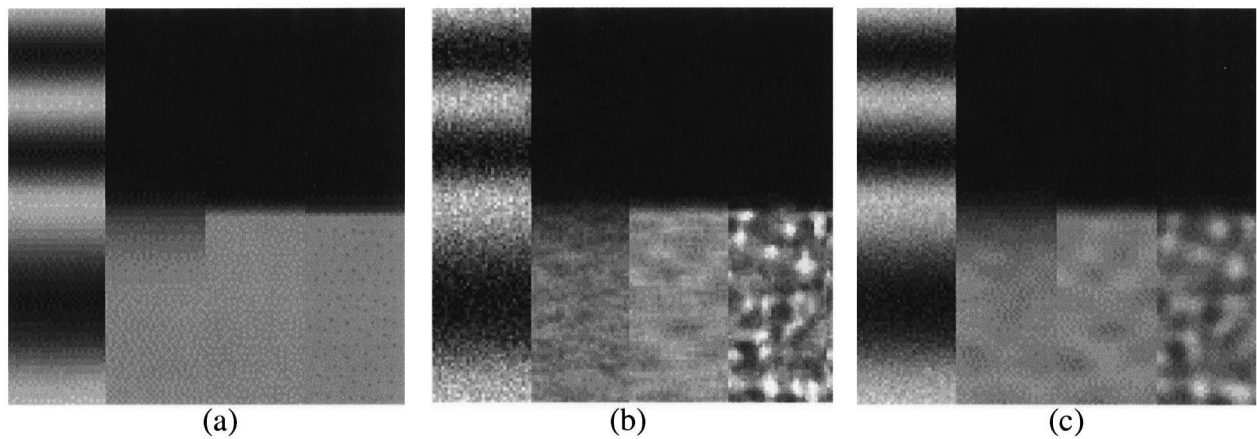
Fig. 4. (a) From left to right: a wave image (at one phase offset) and LFE, phase gradient and AIDE reconstructions for the noiseless two-region data set. (b) The same for the noisy data set. (c) The same for the median filtered data set.

local window, but all simply blur the boundary with no other obvious ill effects.

6.2. Ψ object

To test the ability of the algorithms to recover complex objects, wave data was simulated for a Ψ-shaped object in a slightly heterogeneous background with and without noise. These simulations were calculated using the iterative forward technique described by Dutt et al. (1997). A sample noise-free wave image and images of the amplitude and phase of the harmonic component are shown in Fig. 6. The plane wave is incoming from the left and undergoes significant refraction and interference after interacting with
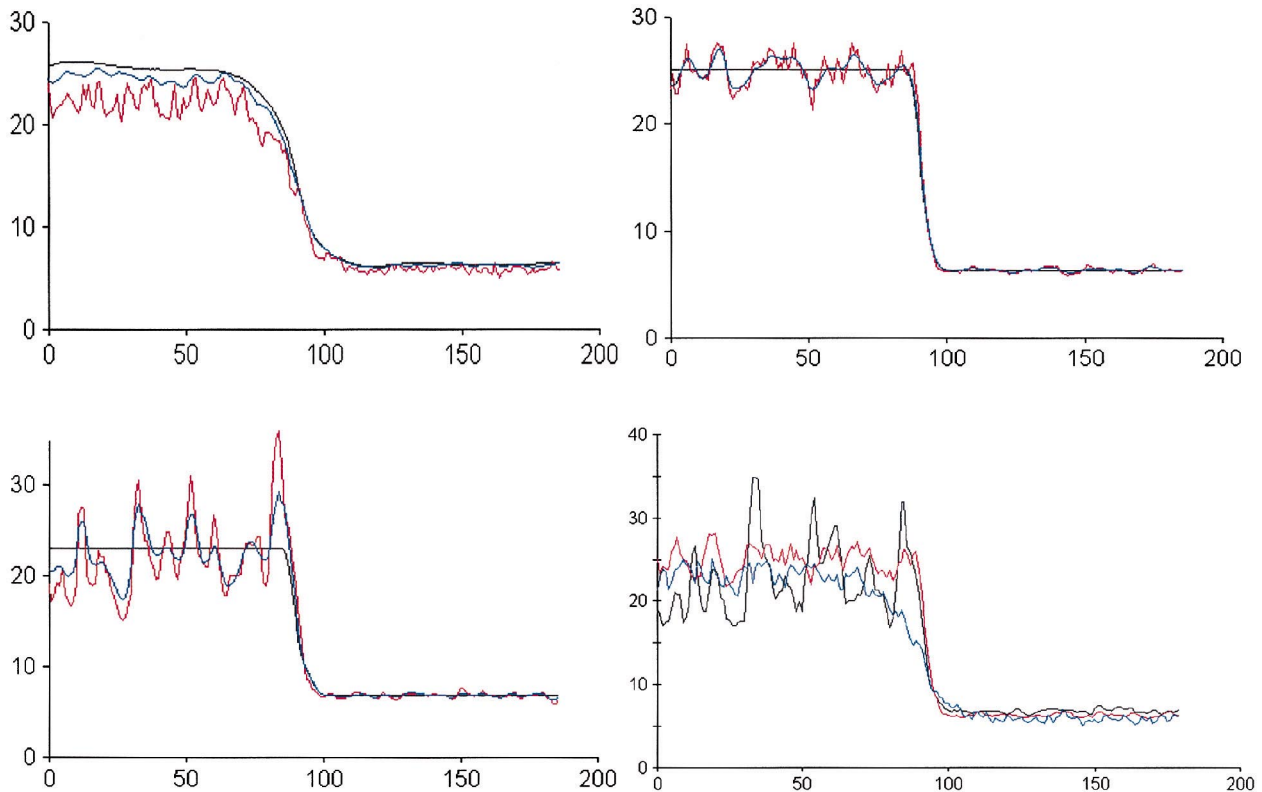
Fig. 5. Vertical profiles through the central columns of the reconstructions in Fig. 4. Top left: the LFE reconstructions for noisy data (red), noise-smoothed data (blue), and noiseless data (black). Top right: the phase gradient reconstructions (same colors). Bottom left: the AIDE reconstructions (same colors). Bottom right: profiles through the reconstructions for the noisy data in Fig. 4(b) for the LFE (blue), phase gradient (red), and AIDE (black) algorithms.
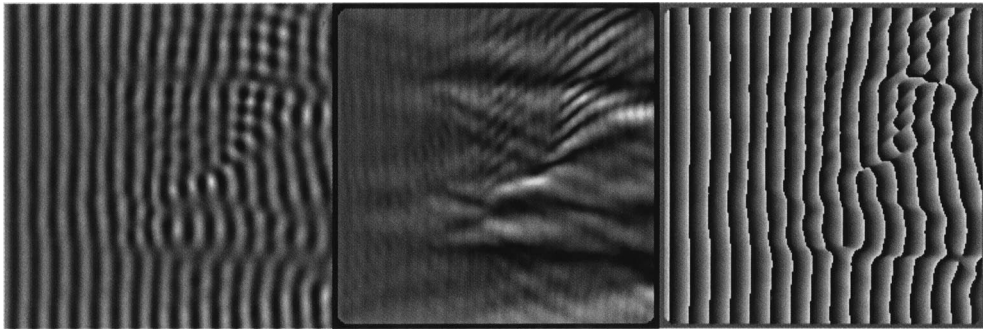
Fig. 6. A wave image from the noiseless synthetic Ψ data set (at one of eight phase offsets), the amplitude of the extracted fundamental component, and its phase. Note the constructive and destructive interference in the amplitude image and the discontinuities in the phase image at amplitude nulls.

the object. Significant amplitude nulls and phase discontinuities are evident. From the wave data alone, there is little clue as to the shape of the object.

Fig. 7 shows the actual shear modulus of the simulated object, and the LFE, phase gradient and AIDE reconstructions. The AIDE reconstruction is sharper than the LFE but has more artifacts and is more affected by the amplitude nulls. The phase gradient algorithm is badly confused by the interfering waves and phase discontinuities even with no noise, and will no longer be discussed, although it

remains useful in specialized situations when a single wave is known to be propagating. Fig. 8 shows a wave image with Gaussian noise (5:1 SNR) and LFE and AIDE reconstructions. The object remains clearly visible but noise artifacts are more pronounced. Once again, the AIDE reconstruction is sharper but more sensitive to noise.

6.3. Prostate phantom

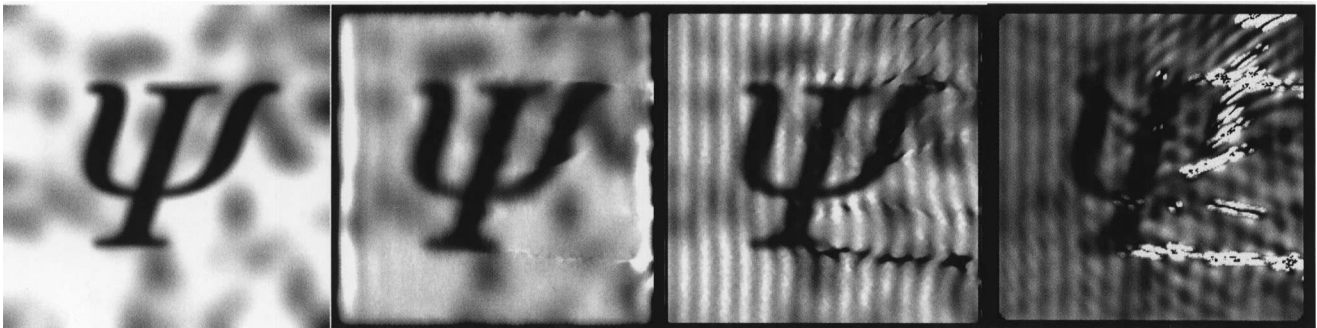A 6 cm diameter cylinder of 1.5% agarose gelatin

Fig. 7. The true shear modulus of the simulated object (left), and the LFE, AIDE and phase gradient reconstructions respectively for the noiseless data. The AIDE reconstruction is sharper than the LFE but has more artifacts and is more affected by the amplitude nulls. The phase gradient result is badly confused by the phase discontinuities.
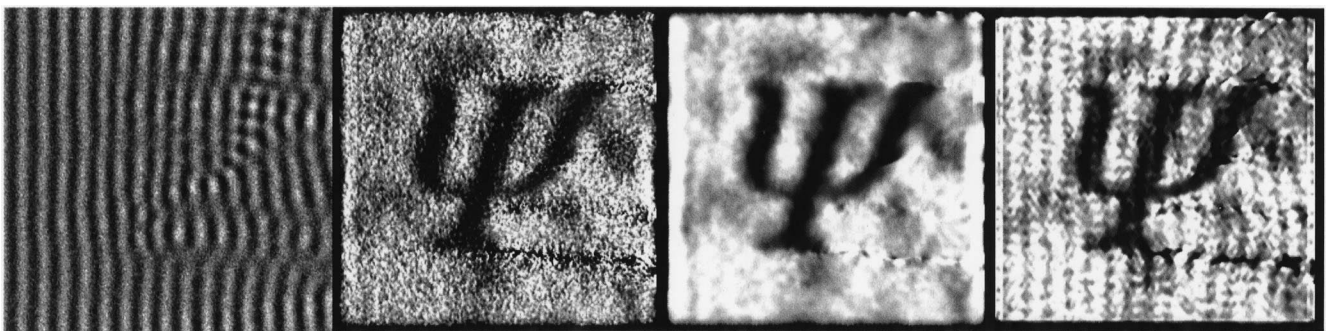

Fig. 8. The noise-added wave image with 5:1 SNR (left), and three reconstructions: the LFE without median filter noise smoothing, with noise smoothing, and the AIDE reconstruction with noise smoothing.

phantom with a 1.4 cm diameter inclusion of 3% gelatin was constructed to simulate a palpable tumor nodule in the peripheral zone of the prostate. Separate large (12 cm diameter cylinders, 12 cm high) phantoms of pure 1.5% and 3% gelatin were constructed from the same batches as
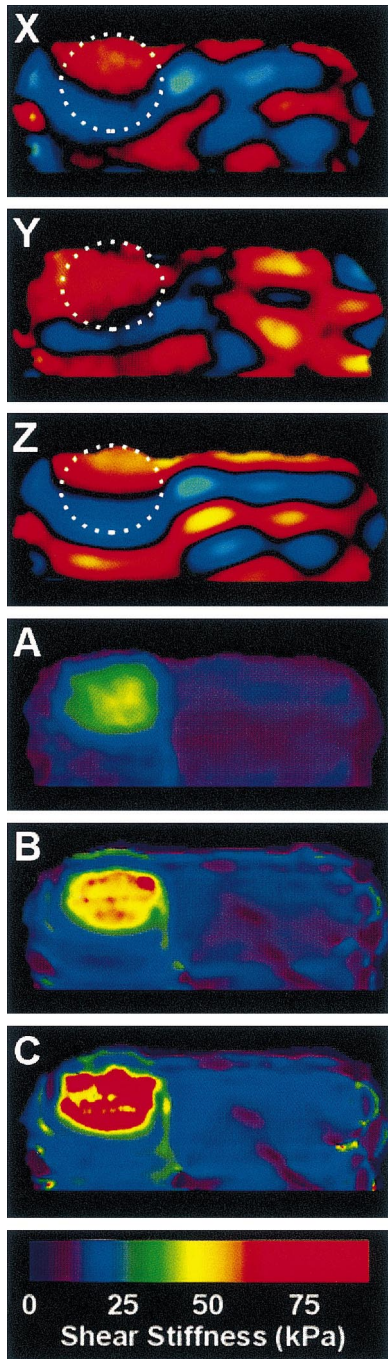
Table 1
Shear stiffness values in the nodule and background regions for three reconstruction techniques and reference values

Region	Method			
	Reference	LFE	AIDE (S–G filters)	AIDE (quadratic fits)
Nodule	56.6±2.1	32.5±2.7	42.8±5.3	60.7±13.5
Background	13.6±0.9	11.8±0.9	12.5±1.4	15.4± 1.8

the tumor phantom as references for determining the true stiffness of the two materials. The phantoms were excited with shear waves at 400 Hz from a plane wave transducer, and full seven-dimensional data was collected of the propagating waves: volume information (3D spatial) about the vector motion (3D motion encoding) through time (eight phase offsets).

The displacement data shows the shear wave propagating through the phantom (Fig. 9), and the outline of the inclusion is obvious. Reconstructions with the LFE and AIDE algorithms are also shown, and averages over regions in the nodule and background are given in Table 1. The LFE and AIDE reconstructions are averages, weighted by amplitude of the harmonic component, of separate reconstructions calculated from the x, y and z displacement data sets. The individual reconstructions (for a single direction of displacement) are similar to but slightly noisier than the averaged results. The reference values were calculated with manual determinations of peak-to-peak distances between the very clean plane waves evident in the reference phantoms. Profiles through the reconstructions are shown in Fig. 10. The LFE result underestimates the true value by almost a factor of two, which is not surprising since the nodule is significantly smaller than a wavelength. The AIDE results have sharper boundaries and are closer to the actual value, but the LFE result is smoother and has fewer artifacts.

In all three test objects, the AIDE reconstructions have higher resolution but are more susceptible to noise and artifacts. The LFE results are smoother but have more limited resolution. The phase gradient technique works

Fig. 9. Performance of inversion algorithms on the prostate phantom. (x,y,z) Wave images with x, y and z motion encoding. Location of stiff nodule shown with dashed circles. (a–c) MR elastograms computed from seven-dimensional data sets: (a) LFE, (b) AIDE algorithm with Savitzky–Golay filters, (c) AIDE algorithm with quadratic fits. The AIDE inversions provide a sharper depiction of the nodule, and a more accurate estimate of its shear stiffness, but are more prone to artifacts.
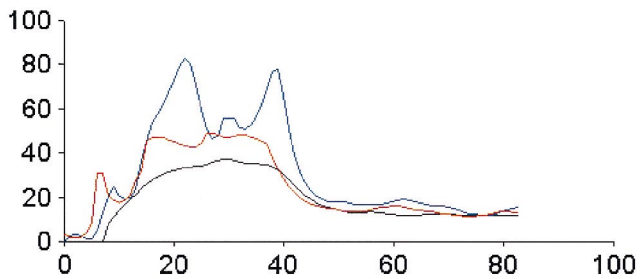

Fig. 10. A vertical profile through the center of the inclusion for the LFE (black), AIDE with Savitzky–Golay filters (red), and AIDE with quadratic fits (blue) reconstructions in Fig. 9 above. The estimated true value for the inclusion from the reference phantom is 56.6 kPa and for the background 13.6 kPa.

well for simple waves but breaks down in more complex scenarios. All three techniques can trade off resolution versus noise sensitivity, either by altering the size of the local window or, in the case of the LFE, by adjusting the filter profiles and central frequencies (Manduca et al., 1996). Techniques that do not assume local homogeneity may yield improved results, but that remains to be proven; it may well be that more important issues are the techniques used for noise smoothing and the estimation of derivatives of noisy data, regardless of the sophistication of the processing algorithm.

7. Experimental results

We briefly summarize some recent results, both ex vivo and in vivo, on both human and animal tissues. All the elastograms shown below are based on LFE processing.

7.1. Animal tissues

A variety of ex vivo experiments have demonstrated that MRE can quantitatively assess the viscoelastic properties of real tissues and detect changes in stiffness with frequency and temperature (Bishop et al., 1998; Kruse et al., 2000). For example, Fig. 11 shows an example of the calculated shear stiffness of porcine liver tissue at different mechanical frequencies. The data are well fit by a viscoelastic model (see Eqs. (8) and (9)). Fig. 12 shows bovine skeletal muscle becoming softer with increasing temperature in the range of 20–45°C. It is recognized that due to the lack of metabolic activity, homeostatis, and in situ preloading in specimens, the observed mechanical
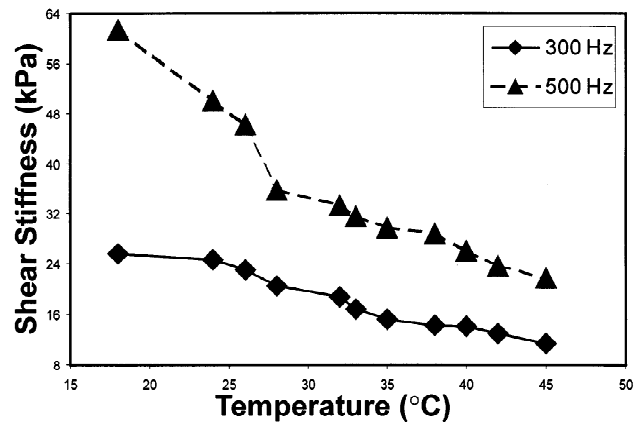
Fig. 12. Shear stiffness measurements obtained using the MR elastography method in a block of bovine skeletal muscle (with heterogeneous fiber orientation). Shear stiffness decreased systematically as the temperature was raised (Kruse et al., 2000).

properties are likely to be different than those that would be measured in vivo.

7.2. Breast

Early work on breast samples with invasive ductal carcinoma obtained after mastectomy yielded elastograms that demonstrated an area of high shear modulus corresponding to the location of the tumor in all specimens (Lawrence et al., 1998). The mean tumor elasticity was $5 \times$ higher than the average shear stiffness of surrounding adipose-fibroglandular tissue. More recent work (Lawrence et al., 1999) has included in vivo imaging of normal volunteers and patients with known cancer. Fig. 13 illustrates wave propagation in the breast of one normal volunteer and clear differentiation between adipose and glandular tissue in the elastogram of another. In patients with tumors, the stiffest regions in the elastogram corresponded to the known tumor locations and were $5–20 \times$ stiffer than normal tissue (Fig. 14). No regions of such high stiffness were found in the normal volunteers. The stiffness values found for the tumors are expected to be an underestimate in all cases, due to the limitations of the processing technique and the scans being 2D instead of 3D. Sinkus et al. (2000) have reported an anisotropic analysis of MRE data of the breast and suggest that this can help differentiate between benign tissue, which appears isotropic, and carcinoma, which appears to exhibit anisotropic elasticity parameters.

7.3. Brain

While there is no clinical precedent for 'brain palpation', it is possible that measurements of elastic properties might be useful for characterizing brain disease. In addition, such measurements are necessary prerequisites for finite element analysis studies of brain trauma and surgical simulation.
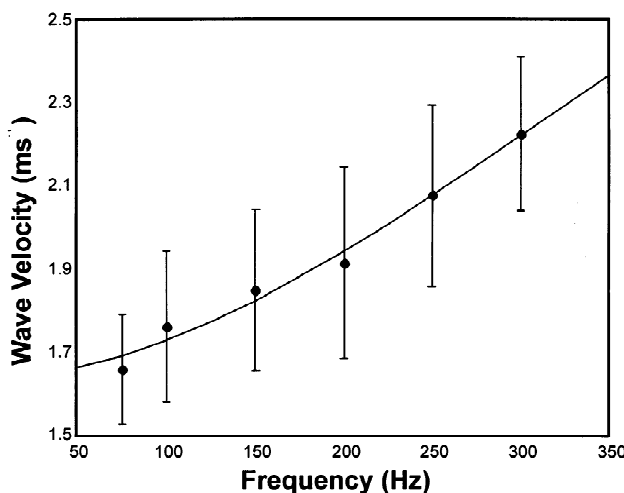

Fig. 11. (a) Shear wave velocity in specimens of porcine liver tissue obtained from five different animals, measured at frequencies of 75–300 Hz. The velocity increases systematically with frequency. The curve represents a best-fit line that accounts for viscoelastic behavior (Kruse et al., 2000).
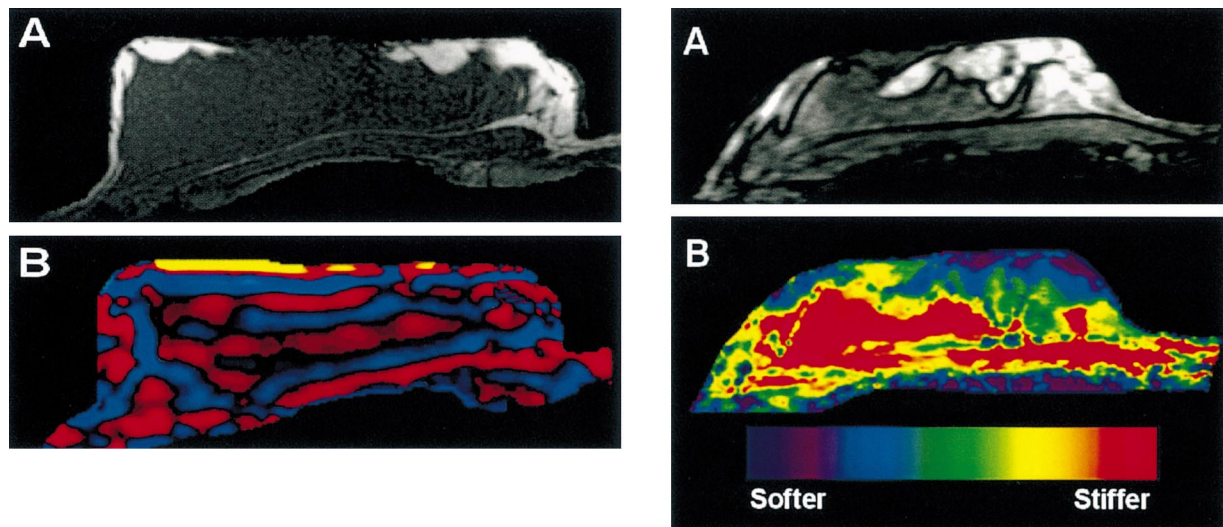
Fig. 13. Left: (a) Axial T1-weighted spin-echo image of the breast of a volunteer with mostly fibroglandular tissue. (b) Wave image demonstrating propagating shear waves in the breast and chest wall. The image was obtained with shear waves at 100 Hz applied to the anterior part of the breast. The motion is in and out of the plane and the waves are propagating toward the chest wall. Right: (a) Axial T1-weighted spin-echo image of the breast of another normal volunteer with more adipose tissue. (b) MR elastogram obtained for this volunteer with shear waves at 100 Hz applied to the anterior part of the breast. The elastogram depicts clear differentiation between soft adipose tissue and stiffer fibroglandular tissue.
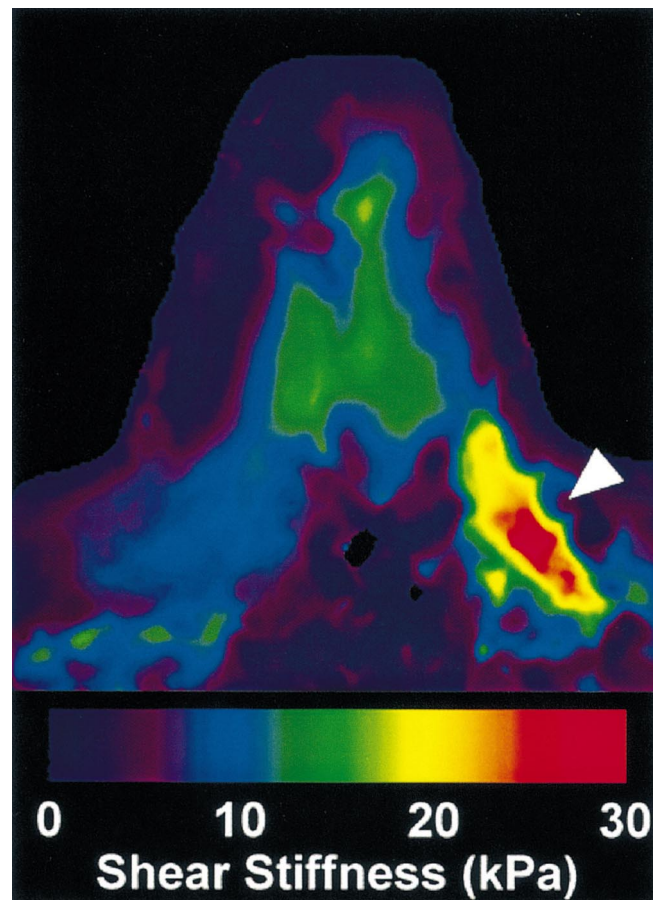

Fig. 14. MR elastogram of the breast of a patient with a 4 cm diameter, biopsy-proven breast cancer. The image was obtained with shear waves at 100 Hz, applied to the skin of the medial and lateral aspects of the breast (Lawrence et al., 1998). The field of view is approximately 16 cm and the section thickness is 5 mm. The MR elastogram indicates that the shear stiffness of the tumor in the posterolateral aspect of the breast (arrowhead) is substantially higher than that of normal fibroglandular and adipose tissues in the breast.

However, the available estimates of the shear modulus of brain tissue in the literature are inconsistent and do not even agree on the relative stiffness of gray and white matter (Galford and McElhaney, 1970; Hirakawa et al., 1981; Nagashima et al., 1990). These estimates were obtained ex vivo, from specimens without blood pressure and metabolic activity. This may explain why they span several orders of magnitude and disagree on whether gray matter is softer or harder than white matter.

Cerebral elastography studies have been performed in normal volunteers (Kruse et al., 1999). Waves are clearly observed to propagate throughout the brain (Fig. 3), and the elastograms (Fig. 15) demonstrate that the in vivo shear stiffness at this frequency of white matter (average value 14.2 kPa) is higher than that of gray matter (average value 5.3 kPa). The difference is statistically significant. No discernable relationship between age and shear modulus has been found.

7.4. Muscle

MRE has been applied to skeletal muscle to quantify the change in stiffness with muscle loading (Dresner et al., 1998). Five volunteers supported varying loads during MRE exams to assess the biceps brachii muscle during active force generation. The wavelength of the shear wave clearly increased with load for each volunteer, as shown in Fig. 16, and in each case the shear stiffness of the muscle rose approximately linearly with force. The slope of the stiffness–force relation varied among the volunteers and was proportional to the inverse of the muscle size.

Muscle tissue is highly anisotropic, and we have found that shear waves propagate preferentially along the muscle fibers. The analysis algorithms presented above all assumed isotropic tissue to reduce the large number of unknown parameters to be estimated. While similar algorithms could be developed without this assumption (Sinkus et al., 2000), solving for the many unknowns would require much larger data sets, probably from a wider variety of experiments that excite different motions, and would be very difficult at best. Indeed, depending on the constitutive equation selected, in some cases parameters may not be determined independently at all, even with a large number of experiments. Our approach to the analysis of muscle data has been to isolate the motion to one type of wave (as above), and then do a simple 1D analysis in the appropriate direction. In the experiments above, this was a damped sinusoid fit to line profiles in the direction of wave propagation.

8. Conclusion

MRE shows great potential for the non-invasive in vivo determination of mechanical properties in a variety of tissues. The detection of propagating acoustic waves has been demonstrated in vivo in breast, brain and muscle and ex vivo in numerous animal and human tissues. Reconstruction algorithms have been tested and characterized
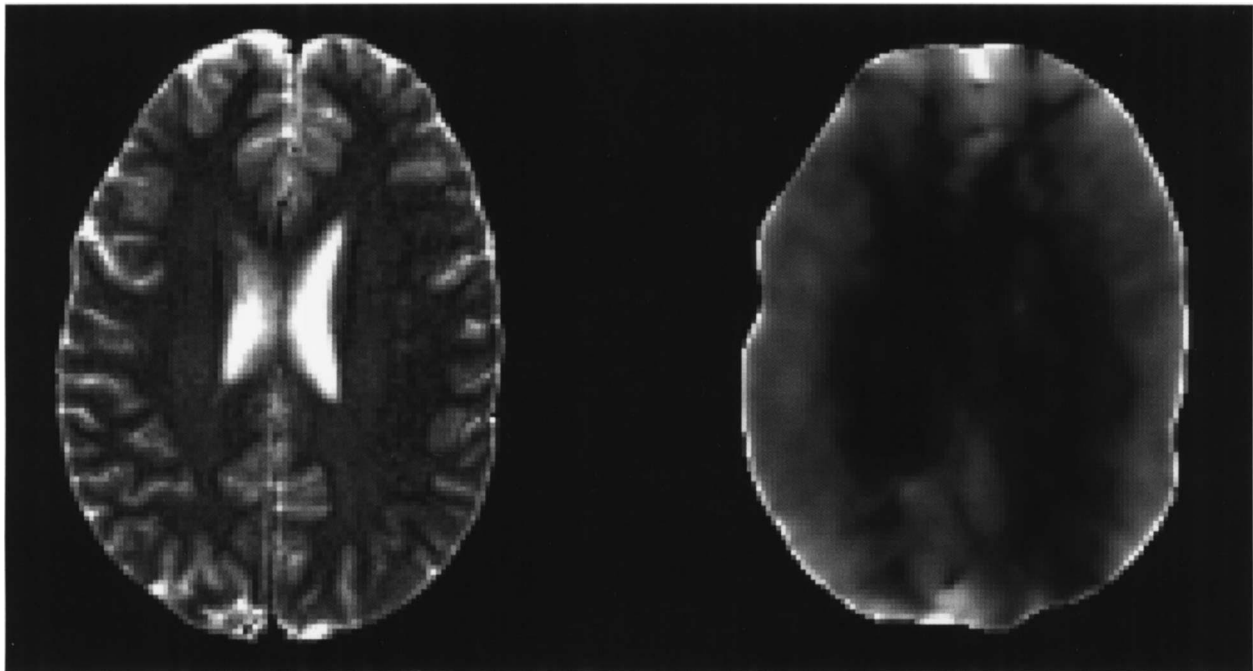

Fig. 15. (Left): T2-weighted spin-echo cerebral image of a volunteer. (Right): Local frequency elastogram (inverse wave speed), showing relative differences between gray and white matter. Shear waves were generated in the brain at 100 Hz by applying lateral motion to a thermoplastic bite bar held in the teeth of the volunteer. One of the wave images from this data set is shown in Fig. 3.
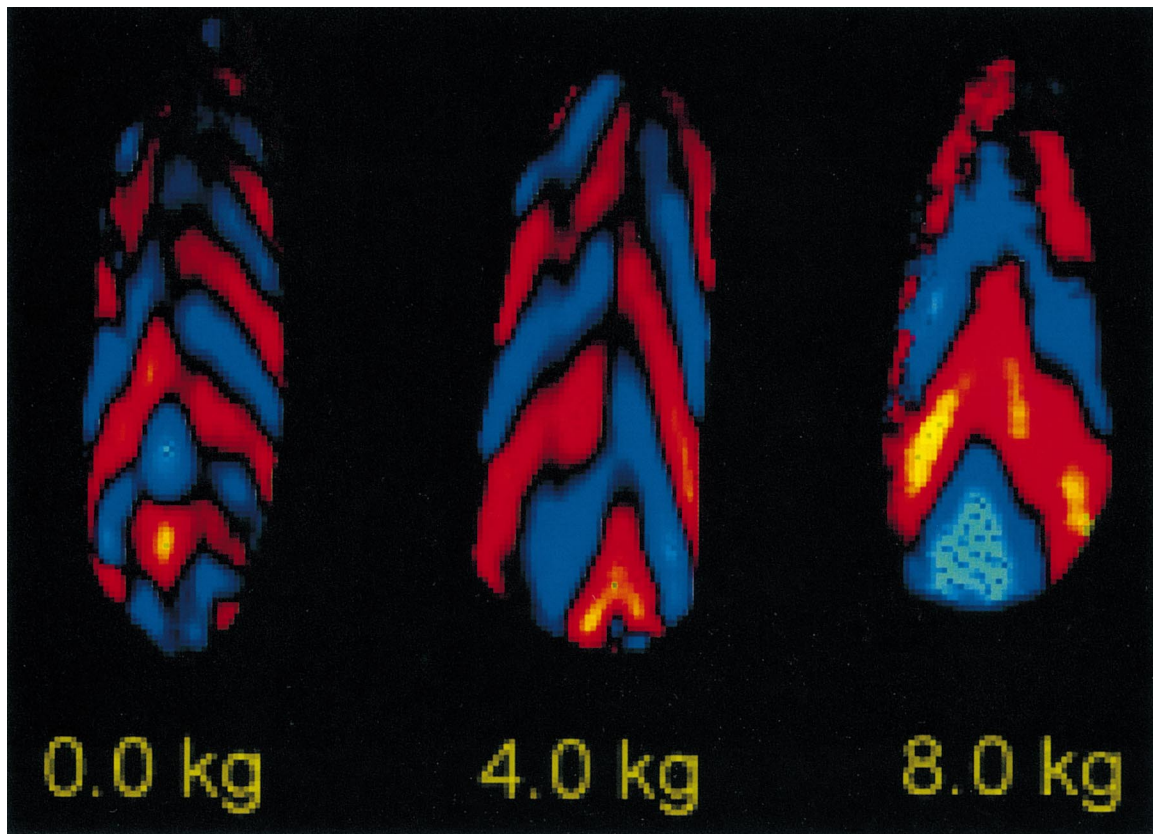
Fig. 16. Wave images obtained in a coronal plane passing through the biceps brachii muscle of a volunteer under the loading conditions indicated. The superior end of the muscle is at the top of the image. Shear waves at 150 Hz were generated in the muscle by an electromechanical driver applied to the skin over the distal biceps tendon (outside the field of view). Section thickness was 7 mm and the field of view of the image is approximately 16 cm. The shear wave image, sensitized for wave motion orthogonal to the plane of section, demonstrates propagating waves, which typically have a chevron-like pattern. The displacement amplitudes are on the order of 30 microns. The shear wavelength clearly increases with load. Preliminary studies have demonstrated a systematic relationship between muscle tension and the speed of the propagating waves (Dresner et al., 1998).

and, although far from perfect, yield quantitative measures of elasticity that clearly demarcate differences between tissue types and identify tumors as areas of higher stiffness. Challenges remain in pulse sequence design, delivering sufficient signal to all areas of the body, and improving processing algorithms to generate more accurate, higher resolution elasticity and attenuation maps. We speculate that MRE may prove to be useful in tumor detection, diseased tissue characterization, and the evaluation of rehabilitation.

Acknowledgements

References

Auld, B.A., 1990. In: Acoustic Fields and Waves in Solids. Krieger, Malabar, FL.

Axel, L., Dougherty, L., 1989. MR imaging of motion with spatial modulation of magnetization. Radiology 171, 841–845.

Bernstein, M.A., Ikezaki, Y., 1991. Comparison of phase-difference and complex-difference processing in phase-contrast MR angiography. JMRI 1, 725–729.

Bishop, J., Poole, G., Leitch, M., Plewes, D.B., 1998. Magnetic resonance imaging of shear wave propagation in excised tissue. JMRI 8, 1257–1265.

Burke, T.M., Blankenberg, T.A., Sui, A.K.Q., Blankenberg, F.G., Jensen, H.M., 1990. Preliminary results for shear wave speed of sound and attenuation coefficients from excised specimens of human breast tissue. Ultrason. Imag. 12, 99–118.

Burlew, M.M., Madsen, E.L., Zagzebski, J.A., Banjavic, R.A., Sum, S.W., 1980. A new ultrasound tissue-equivalent material. Radiology 134 (2), 517–520.

Catheline, S., Wu, F., Fink, M., 1999. A solution to diffraction biases in sonoelasticity: the acoustic impulse technique. J. Acoust. Soc. Am. 105, 2941–2950.

Cespedes, I., Ophir, J., Ponnekanti, H., Maklad, N., 1993. Elastography: elasticity imaging using ultrasound with application to muscle and breast in vivo. Ultrason. Imag. 15, 73–88.

Dresner, M.A., Rose, G.H., Rossman, P.J., Smith, J.A., Muthupillai, R., Ehman, R.L., 1998. Functional MR elastography of human skeletal muscle. In: Proceedings of the International Society of Magnetic Resonance in Medicine, p. 463.

Dutt, V., Muthupillai, R., Manduca, A., Ehman, R.L., Greenleaf, J.F.,

1997. Inverse approach to elasticity reconstruction in shear wave imaging. In: Proceedings of the 1997 IEEE Ultrasonics Symposium, pp. 1415–1418.

Ehrichs, E.E., Jaeger, H.M., Karczmar, G.S., Knight, J.B., Kuperman, V.Y., Nagel, S.R., 1995. Granular convection observed by magnetic resonance imaging. Science 267, 1632–1634.

Fowlkes, J.B., Emelianov, S.Y., Pipe, J.G., Skovoroda, A.R., Carson, P.L., Adler, R.S., Sarvazyan, A.P., 1995. Magnetic-resonance imaging techniques for detection of elasticity variation. Med. Phys. 22 (11), 1771–1778.

Fung, Y.C., 1993. In: Biomechanics – Mechanical Properties of Living Tissues, 2nd Edition. Springer, New York.

Galford, J.E., McElhaney, J.H., 1970. A viso-elastic study of scalp, brain and dura. J. Biomech. 3, 211–221.

Gao, L., Parker, K.J., Alam, S.K., 1995. Sonoelasticity imaging: theory and experimental verification. J. Acoust. Soc. Am. 97, 3875–3885.

Gao, L., Parker, K.J., Lerner, R.M., Levinson, S.F., 1996. Imaging of the elastic properties of tissue – a review. Ultrasound Med. Biol. 22, 959–977.

Garra, B.S., Cespedes, E.I., Ophir, J., Spratt, S.R., Zuurbier, R.A., Magnant, C.M., Pennanen, M.F., 1997. Elastography of breast lesions: initial clinical results. Radiology 202 (1), 79–86.

Ghiglia, D.C., Pritt, M.D., 1998. Two-Dimensional Phase Unwrapping: Theory, Algorithms and Software. Wiley, New York.

Goss, S.A., Johnston, R.L., Shnol, S.E., 1978. Comprehensive compilation of empirical ultrasonic properties of mammalian tissues. J. Acoust. Soc. Am. 64 (2), 423–457.

Hirakawa, K., Hashizume, K., Hayashi, T., 1981. Viscoelastic property of human brain — for the analysis of impact injury. No To Shinkei 33 (10), 1057–1065.

Huang, S.R., Roach, D.J., 1991. Sonoelasticity imaging: results in in vitro tissue specimens. Radiology 181, 237–239.

Kallel, F., Bertrand, M., 1996. Tissue elasticity reconstruction using linear perturbation method. IEEE Trans. Med. Imag. 15 (3), 299–313.

Knutsson, H., Westin, C.J., Granlund, G., 1994. Local multiscale frequency and bandwidth estimation. In: Proceedings of the IEEE International Conference on Image Processing, pp. 36–40.

Krouskop, T.A., Dougherty, D.A., Vinson, F.S., 1987. A pulsed Doppler ultrasonic system for making noninvasive measurements of the mechanical properties of soft tissue. J. Rehabil. Res. Dev. 24 (2), 1–8.

Krouskop, T.A., Wheeler, T.M., Kallel, F., Garra, B.S., Hall, T., 1998. Elastic moduli of breast and prostate tissues under compression. Ultrason. Imag. 20 (4), 260–274.

Kruse, S.A., Dresner, M.A., Rossman, P.J., Felmlee, J.P., Jack, C.R., Ehman, R.L., 1999. 'Palpation of the brain' using magnetic resonance elastography. Proc. Int. Soc. Magn. Reson. Med. 7, 258.

Kruse, S.A., Smith, J.A., Lawrence, A.J., Dresner, M.A., Manduca, A., Greenleaf, J.F., Ehman, R.L., 2000. Tissue characterization using magnetic resonance elastography: preliminary results. Phys. Med. Biol. 45, 1579–1590.

Lawrence, A.J., Muthupillai, R., Rossman, P.J., Smith, J.A., Manduca, A., Ehman, R.L., 1998. MR elastography of the breast: preliminary results. Proc. Int. Soc. Magn. Reson. Med. 6, 233.

Lawrence, A.J., Rossman, P.J., Mahowald, J.L., Manduca, A., Hartmann, L.C., Ehman, R.L., 1999. Assessment of breast cancer by magnetic resonance elastography. Proc. Int. Soc. Magn. Reson. Med. 7, 525.

Lee, F.J., Bronson, J.P., Lerner, R.M., Parker, K.J., Huang, S.R., Roach, D.J., 1991. Sonoelasticity imaging: results in in vitro tissue specimens. Radiology 181, 237–239.

Lerner, R.M., Huang, S.R., Parker, K.J., 1990. Sonoelasticity images derived from ultrasound signals in mechanically vibrated tissues. Ultrasound Med. Biol. 16, 231–239.

Manduca, A., Muthupillai, R., Rossman, P.J., Greenleaf, J.F., Ehman, R.L., 1996. Image processing for magnetic resonance elastography. SPIE Med. Imag. 2710, 616–623.

Manduca, A., Smith, J.A., Muthupillai, R., Rossman, P.J., Greenleaf, J.F., Ehman, R.L., 1997a. Image analysis techniques for magnetic resonance elastography. Proc. Int. Soc. Magn. Reson. Med. 5, 1905.

Manduca, A., Muthupillai, R., Rossman, P.J., Greenleaf, J.F., Ehman, R.L., 1997b. 3-D local wavelength estimation for magnetic resonance elastography. Radiology 205 (P), 469.

Muthupillai, R., Ehman, R.L., 1997. Amplitude modulated cyclic gradient waveforms: application in MR elastography. Proc. Int. Soc. Magn. Reson. Med. 5, 1904.

Muthupillai, R., Lomas, D.J., Rossman, P.J., Greenleaf, J.F., Manduca, A., Ehman, R.L., 1995. Magnetic resonance elastography by direct visualization of propagating acoustic strain waves. Science 269, 1854–1857.

Muthupillai, R., Rossman, P.J., Lomas, D.J., Greenleaf, J.F., Riederer, S.J., Ehman, R.L., 1996a. Magnetic resonance imaging of transverse acoustic strain waves. Magn. Reson. Med. 36, 266–274.

Muthupillai, R., Rossman, P.J., Greenleaf, J.F., Riederer, S.J., Ehman, R.L., 1996b. MRI visualization of acoustic strain waves: effect of linear motion. Proc. Int. Soc. Magn. Reson. Med. 4, 1515.

Muthupillai, R., Dutt, V., Rossman, P.J., Hulshizer, T.C., Manduca, A., Ehman, R.L., 1997. Three dimensional magnetic resonance elastography with multi-axis motion encoding. Proc. Int. Soc. Magn. Reson. Med. 5, 460.

Nagashima, T., Shirakuni, T., Rapopart, S.I., 1990. A two-dimensional, finite element analysis of vasogenic brain edema. Neurol. Med.-Chir. 30, 1–9.

O'Donnell, M., 1985. NMR blood flow imaging using multiecho, phase contrast sequences. Med. Phys. 12, 59–64.

O'Donnell, M., Skovoroda, A.R., Shapo, B.M., Emellanov, S.Y., 1994. Internal displacement and strain imaging using ultrasonic speckle tracking. IEEE Trans. Ultrason. Ferroelect. Freq. Cntrl. 41, 314–325.

Oliphant, T.E., Mahowald, J.L., Ehman, R.L., Greenleaf, J.F., 1999. Complex-valued quantitative stiffness estimation using dynamic displacement measurements and local inversion of conservation of momentum. In: IEEE International Ultrasonics Symposium, Lake Tahoe, NV.

Oliphant, T.E., Manduca, A., Ehman, R.L., Greenleaf, J.F., 2000. Complex-valued stiffness reconstruction for magnetic resonance elastography by algebraic inversion of the differential equation. Magn. Reson. Med. (in press).

Ophir, J., Cespedes, I., Ponnekanti, H., Yazdi, Y., Li, X., 1991. Elastography: a quantitative method for imaging the elasticity of biological tissues. Ultrason. Imag. 13, 111–134.

Parker, K., Lerner, R., 1992. Sonoelasticity of organs: shear waves ring a bell. J. Ultrasound Med. 11, 387–392.

Parker, K.J., Huang, S.R., Musulin, R.A., Lerner, R.M., 1990. Tissue response to mechanical vibrations for sonoelasticity imaging. Ultrasound Med. Biol. 16 (3), 241–246.

Pelc, N.J., Shimakawa, A., Glover, G.H., 1989. Phase contrast cine MRI. Annu. Meet. Soc. Magn. Reson. Med. 1, 101.

Plewes, D.B., Betty, I., Urchuk, S.N., Soutar, I., 1994. Visualizing tissue compliance with MR. In: Second Annual Meeting, Society of Magnetic Resonance.

Plewes, D.B., Betty, I., Urchukm, S.N., Soutar, I., 1995. Visualizing tissue compliance with MR imaging. JMRI 5, 733–738.

Ponnekanti, H., Ophir, J., Cespedes, I., 1992. Axial stress distributions between coaxial compressors in elastography: an analytical model. Ultrasound Med. Biol. 18 (8), 667–673.

Ponnekanti, H., Ophir, J., Cespedes, I., 1994. Ultrasonic imaging of the stress distribution in elastic media due to an external compressor. Ultrasound Med. Biol. 20 (1), 27–33.

Ponnekanti, H., Ophir, J., Huang, Y., Cespedes, I., 1995. Fundamental mechanical limitations on the visualization of elasticity contrast in elastography. Ultrasound Med. Biol. 21 (4), 533–543.

Press, W.H., Teukolsky, S.A., Vetterling, W.T., Flannery, B.P., 1992. In: Numerical Recipes in C. Cambridge University Press, New York.

Romano, A.J., Shirron, J.J., Bucaro, J.A., 1998. On the noninvasive determination of material parameters from a knowledge of elastic displacements: theory and numerical simulation. IEEE Trans. Ultrason. Ferroelect. Freq. Cntrl. 45 (3), 751–759.

Rubens, D.J., Hadley, M.A., Alam, S.K., Gao, L., Mayer, R.D., Parker, K.J., 1995. Sonoelasticity imaging of prostate cancer: in vitro results. Radiology 195, 379–383.

Sarvazyan, A., Goukassian, D., Maevsky, G., 1994. Elasticity imaging as a new modality of medical imaging for cancer detection. In: Proceedings of an International Workshop on Interaction of Ultrasound with Biological Media, pp. 69–81.

Sinkus, R., Lorenzen, J., Schrader, D., Lorenzen, M., Dargatz, M., Holz, D., 2000. High-resolution tensor MR elastography for breast tumour detection. Phys. Med. Biol. 45, 1649–1664.

Van Houten, E.E.W., Paulsen, K.D., Miga, M.I., Kennedy, F.E., Weaver, J.B., 1999. An overlapping subzone technique for MR-based elastic property reconstruction. Magn. Reson. Med. 42, 779–786.

Wu, T., Felmlee, J.P., Greenleaf, J.F., Riederer, S.J., Ehman, R.L., 2000. MR imaging of shear waves generated by focused ultrasound. Magn. Reson. Med. 43, 111–115.

Yamakoshi, Y., Sato, J., Sato, I., 1990. Ultrasound imaging of internal vibration of soft tissue under forced vibration. IEEE Trans. Ultrason. Ferroelect. Freq. Cntrl. 37, 45–53.

Zerhouni, E.A., Parish, D.M., Rogers, W.J., Yang, A., Shapiro, E.P., 1988. Human heart: tagging with MR imaging — a method for noninvasive assessment of myocardial motion. Radiology 169, 59–63.